Vicia faba TPC1, a genetically encoded variant of the vacuole Two Pore Channel 1, is hyperexcitable

Jinping Lu[1], Ingo Dreyer[2], Miles Sasha Dickinson[3], Sabine Panzer[4], Dawid Jaslan[1,5], Carlos Navarro-Retamal[2], Dietmar Geiger[1], Ulrich Terpitz[4], Dirk Becker[1], Robert M. Stroud*[3], Irene Marten*[1], Rainer Hedrich[1]

[1] Department of Molecular Plant Physiology and Biophysics, Biocenter, University of Würzburg, D-97082 Würzburg, Germany

[2] Center of Bioinformatics, Simulation and Modeling, Faculty of Engineering, Universidad de Talca, 3460000 Talca, Chile

[3] Department of Biochemistry and Biophysics, University of California San Francisco, San Francisco, CA 94143, U.S.A.

[4] Theodor-Boveri-Institute, Department of Biotechnology and Biophysics, Biocenter, University of Würzburg, D-97074 Würzburg, Germany

[5] Walther Straub Institute of Pharmacology and Toxicology, Faculty of Medicine, Ludwig Maximilians-Universität, 80336 Munich, Germany

*Corresponding authors

Abstract

To fire action-potential-like electrical signals, the vacuole membrane requires the depolarization-activated two-pore channel TPC1, also called Slowly activating Vacuolar SV channel. The TPC1/SV channel, encoded by the *TPC1* gene, functions as a voltage-dependent and Ca^{2+}-regulated potassium channel. TPC1 currents are activated by a rise in cytoplasmic Ca^{2+} but blocked by luminal Ca^{2+}. In search for species-dependent functional TPC1 channel variants, we studied polymorphic amino acids contributing to luminal Ca^{2+} sensitivity. We found that the acidic residues Glu457, Glu605 and Asp606 of the Ca^{2+}-sensitive Arabidopsis AtTPC1 channel were neutralized by either asparagine or alanine in *Vicia faba* and many other Fabaceae as well. When expressed in the Arabidopsis loss-of-AtTPC1 function background, the wild type VfTPC1 was hypersensitive to vacuole depolarization and insensitive to blocking luminal Ca^{2+}. When AtTPC1 was mutated for the three VfTPC1-homologous polymorphic site residues, the Arabidopsis At-VfTPC1 channel mutant gained VfTPC1-like voltage and luminal Ca^{2+} insensitivity that together made vacuoles hyperexcitable. These findings indicate that natural TPC1 channel variants in plant families exist which differ in vacuole excitability and very likely respond to changes in environmental settings of their ecological niche.

Introduction

Soon after the patch-clamp technique was first applied to plant cells (for review see (Schroeder and Hedrich, 1989), the slow vacuolar SV channel was identified as a calcium-regulated, voltage-dependent cation channel (Hedrich and Neher, 1987). After two further decades it was demonstrated in *Arabidopsis thaliana* that the SV channel is encoded by the single copy gene *TPC1* (Peiter et al., 2005). TPC1 contributes to long-distance electrical and Ca^{2+} signaling and is an essential player in vacuole excitability (Choi et al., 2014; Evans et al., 2016; Jaslan et al., 2019).

Cation replacement experiments with vacuoles isolated from *Vicia faba* plants have shown that the SV/TPC1 channel is able to conduct not only the monovalent K^+ and Na^+ but also Ca^{2+} ions. Under non-physiological solute conditions for K^+ and Ca^{2+} in the cytosol and Ca^{2+} as the only cation in the vacuole, the SV/TPC1 channel was found 5-fold more permeable for Ca^{2+} than K^+ (Ward and Schroeder, 1994). However, when investigated under physiological, plant cell-like Ca^{2+} and K^+ concentrations and gradients, the SV/TPC1 channel was predominately conducting K^+ (Schulz-Lessdorf and Hedrich, 1995; for review see Hedrich and Marten, 2011; Hedrich et al., 2018). Interestingly, the Arabidopsis TPC1 channel homolog is blocked when Ca^{2+} in the vacuole lumen is elevated (Dadacz-Narloch et al., 2011). As a consequence, luminal Ca^{2+} concentrations around 1 mM (in the presence of 100 mM K^+) prevent vacuole excitation (Jaslan et al., 2019) suggesting that the SV/TPC1 channel does not serve as a vacuolar Ca^{2+} release channel.

Within the tree of live, there are TPC1-like sequences in animals and plants (see for review (Kintzer and Stroud, 2018; Jaslan et al., 2020). Remarkably, during land plant evolution characteristic structural fingerprints of TPC1-type channels remained unchanged from mosses to flowering plants (Hedrich et al., 1988; Dadacz-Narloch et al., 2011; Dreyer et al., 2021). Recently, both the crystal and cryoEM structure of the Arabidopsis AtTPC1 channel and thus the molecular topology of this vacuolar cation channel became available (Guo et al., 2016; Kintzer and Stroud, 2016). AtTPC1 is formed by a dimer whose monomers consist of two tandem Shaker-like cassettes, each with six transmembrane domains (TM1-6), connected by a cytoplasmic loop with two EF hands. Calcium binding to the EF hands is necessary for SV/TPC1 channel activation at elevated cytosolic Ca^{2+} levels (Schulze et al., 2011). Structural 3D motif comparison and point mutation analysis identified the major voltage-sensing domain (VSD) required for depolarization-dependent activation in each monomer in the first

four transmembrane segments of the second Shaker-like cassette (Guo et al., 2016; Jaslan et al., 2016). On a similar experimental basis, it was found that Ca^{2+} binding to the EF hands addresses the voltage-sensing domain and opens the channel gate (Schulze et al., 2011; Guo et al., 2016). This is not the case when the Ca^{2+} level in the vacuolar lumen reaches 1 mM and more (Jaslan et al., 2019). Luminal Ca^{2+} can bind to two non-canonical calcium binding sites each formed by three acidic residues (site 1, Asp240/Asp454/Glu528; site 2, Glu239/Asp240/Glu457) (Guo et al., 2016; Kintzer and Stroud, 2016). Among them, site 1 appears to represent the major luminal Ca^{2+} inhibition site including the central residue Asp454 placed in the luminal loop between transmembrane domains 7 and 8 (Guo et al., 2016; Kintzer and Stroud, 2016). In addition, luminal Ca^{2+} binding also appears to occur in the luminal pore region of AtTPC1 over Glu605 and Asp606, affecting voltage gating and likely luminal Ca^{2+} inhibition (Kintzer and Stroud, 2016; Kintzer et al., 2018; Dickinson et al., 2022).

In a screening with chemically induced Arabidopsis mutants for plants that produce elevated amounts of the wound hormone jasmonate (JA), the mutation *fou2* in the TPC1 channel was identified (Bonaventure et al., 2007b). Interestingly, *fou2* behaves like a hyperactive TPC1 channel (Bonaventure et al., 2007b; Beyhl et al., 2009). While wild type AtTPC1 becomes active when the vacuole membrane depolarizes, the *fou2* channel opens already near the resting membrane voltage. As a consequence, the *fou2* vacuole must experience episodes in which the membrane potential is short-circuited and thus appears wounded and produces large amounts of jasmonate. Despite this hyperactivity, a stress signal-induced rise in the cytoplasmic Ca^{2+} level does not differ between wild type Arabidopsis plants and the *fou2* mutant (Lenglet et al., 2017) supporting further the notion that TPC1 does not serve as a vacuolar Ca^{2+} release channel. The hypersensitivity of the *fou2* channel towards voltage results from a mutation of the negatively charged glutamate at position 454 to the uncharged asparagine (D454N). This TPC1 site is directed towards the vacuole lumen and is part of the non-canonical Ca^{2+} sensor (Dadacz-Narloch et al., 2011; Guo et al., 2016; Kintzer and Stroud, 2016). Elevated luminal Ca^{2+} levels block the activity of wild type TPC1 channels but not of the *fou2* mutant channel (Lenglet et al., 2017). Thus, the D454N mutation desensitizes AtTPC1 towards vacuolar Ca^{2+}, which physiologically results in an increased amount of stored Ca^{2+} in the vacuole (Beyhl et al., 2009) and a gene expression pattern reminiscent to plants suffering from potassium starvation (Bonaventure et al., 2007a). Structural modeling in the context of the *fou2* mutation

site showed that additional amino acids other than the central Ca^{2+} binding sites like Asp454 are important for luminal Ca^{2+} sensitivity, e.g. the adjacent Glu456 and Glu457 (Dadacz-Narloch et al., 2011). SV/TPC1 channels lacking any of these three negatively charged residues appeared altered in Ca^{2+} sensitivity of channel gating indicating that Glu456 and Glu457 might connect the luminal Ca^{2+} binding site to the channel gate (Dadacz-Narloch et al., 2011).

The TPC1 channels from *Vicia faba* and *Arabidopsis thaliana* are historically established prototypes of the SV channel type. Nevertheless, only AtTPC1 but not VfTPC1 has been identified at the molecular level so far. In this study, we therefore cloned VfTPC1 and analyzed its electrical properties compared with AtTPC1 after expression in the Arabidopsis *tpc1-2* null allele mutant. Despite similarities, these two TPC1 channel types showed also astonishing differences, especially with respect to their luminal Ca^{2+} dependency. In search for the structural reasons for this divergence, we could pinpoint three polymorphic sites within two luminal Ca^{2+} coordinating regions. When these polymorphic sites were implemented into the Arabidopsis TPC1 channel, AtTPC1 was converted into a hyperactive SV/TPC1 channel desensitized to luminal Ca^{2+}, mimicking the properties of VfTPC1 and the AtTPC1 mutant *fou2*. This suggests that within the green tree of life, polymorphisms in TPC1 may allow species to adapt the electrical properties of the vacuole to given individual settings.

Results

VfTPC1 is a native hyperactive TPC1 channel variant with a low luminal Ca^{2+} sensitivity

In our search for natural TPC1 channel variants, we noticed that SV currents have been recorded from *Vicia faba* guard cell vacuoles even under extremely high luminal Ca^{2+} loads (50 mM; Ward and Schroeder, 1994). Considering that in *Arabidopsis thaliana* mesophyll vacuoles hardly any AtTPC1/SV currents were present even at lower luminal Ca^{2+} levels (10 mM; Lenglet et al., 2017), the TPC1 channel variants of *Vicia faba* and *Arabidopsis thaliana* seem to differ in their luminal Ca^{2+} sensitivity. To prove this assumption, we compared these TPC1 channel types with respect to their function and structure. In contrast to *TPC1* from *Arabidopsis thaliana* (Peiter et al. 2005), the *VfTPC1* gene has not yet been identified, and proper sequence information of the giant faba bean genome (~13 Gb) was also not available. In order to nevertheless gain insights into the molecular structure and function of VfTPC1, we isolated the RNA from bean leaves and epidermis with only stomatal guard cells alive. Following RNA-seq and *de novo* transcriptome assembly of both samples, we identified a single *VfTPC1* transcript (Genbank MW380418), just as in *Arabidopsis thaliana* (Peiter et al. 2005).

After VfTPC1 was cloned and fused to a eYFP tag, mesophyll protoplasts isolated from the Arabidopsis TPC1-loss-of-function mutant *tpc1-2* were transiently transformed with the fava bean TPC1 channel. Similar to TPC1 from Arabidopsis (Fig. S1) and other plant species (Dadacz-Narloch et al., 2013), VfTPC1 was found to localize exclusively to the vacuole membrane as visualized by the fluorescent eYFP signal (Fig. S1). In the following, patch clamp experiments were conducted with fluorescent mesophyll vacuoles to study the functional features of the VfTPC1 channel. Following application of a vacuole-releasing solution, protoplasts collapsed, and the vacuole membrane became accessible for patch pipettes (cf. Schulz-Lessdorf and Hedrich, 1995; Lagostena et al., 2017). When the whole-vacuole configuration was established under symmetrical 150 mM K^+ conditions, depolarizing voltage pulses elicited macroscopic outward-rectifying SV/TPC1-like currents (Fig. 1A), demonstrating the functionality of VfTPC1. However, compared to AtTPC1, VfTPC1 channels differed in kinetics, voltage dependence and luminal calcium sensitivity (Figs. 1, 2, S2, S3).

In the absence of luminal Ca^{2+}, the current activation was faster and the current deactivation slower with VfTPC1 than with AtTPC1 (Figs. 1a, S2a, b, S3a, b). A closer look at the current-voltage curves further revealed that besides the outward currents,

inward currents were also elicited upon voltage pulses in the range of -40 and 0 mV but only from vacuoles that harbored VfTPC1 and not AtTPC1 (Fig. S4a). This points to a shift in the voltage activation threshold for VfTPC1 channel opening by about 30 mV to more negative voltages and thus close to the vacuolar resting membrane voltage. For further quantification of this effect, the voltage-dependent relative open-channel probability curves ($G/G_{max}(V)$) were determined for both TPC1 type channels (Fig. 2a). They were fitted with a double Boltzmann equation describing the voltage-dependent channel transitions between two closed and one open state ($C_2 \leftrightarrows C_1 \leftrightarrows O$) (Pottosin et al., 2004; Jaslan et al., 2016), and from these fits the midpoint voltages V_2 and V_1 were derived (Fig. 2b). In line with the different activation threshold of the TPC1 currents, in particular the midpoint voltage V_1 of VfTPC1 (-3.5 ± 12.3 mV, n=5) was more negative compared to that of AtTPC1 (51.2 ± 9.6 mV, n=5), confirming a significant difference in voltage gating between these channel types (Fig. 2b).

When the luminal Ca^{2+} concentration was increased from 0 to 10 mM Ca^{2+}, the activation kinetics of AtTPC1 was strongly slowed down. At +90 mV, for example, the half-activation time increased by about 170% (Fig. S2a-c, e, f). In contrast, the Ca^{2+} effect on the activation kinetics of VfTPC1 was less pronounced. At +90 mV, the half-activation time of VfTPC1 currents increased by only about 53%, and at 10 and 50 mM Ca^{2+} the half-deactivation time was still larger than that of AtTPC1 (Figs. S3, S4). Even more impressive was that the AtTPC1 currents were suppressed by about 50% at 10 mM luminal Ca^{2+} and even completely blocked when further raised to 50 mM luminal Ca^{2+} (Fig. 1). In contrast, the VfTPC1 current densities at zero and 10 mM luminal Ca^{2+} did not differ in this magnitude, and at 50 mM Ca^{2+} the VfTPC1 current density still reached about 50% of the level measured under luminal Ca^{2+}-free conditions. The strongly reduced susceptibility of VfTPC1 currents to inhibitory luminal Ca^{2+} ions was associated with a significantly reduced inhibitory effect on voltage activation (Fig. 2). Compared to 0 mM Ca^{2+}, at 10 mM Ca^{2+} the V_1 and V_2 values increased by about 115 mV and 61 mV for AtTPC1, but only by about 61 mV and 26 mV for VfTPC1, respectively (Fig. 2b, c). A rise from 10 to 50 mM luminal Ca^{2+} caused a further positive-going shift of the VfTPC1 activation voltage curve ($G/G_{max}(V)$), indicated by a 1.7- and 1.6-fold rise in V_1 and V_2, respectively (Fig. 2B). In comparison, the AtTPC1 currents, were so small at 50 mM luminal Ca^{2+} (Fig. 1) that activation voltage curves ($G/G_{max}(V)$) could not be resolved reliably. Taken together, these results clearly document that, compared to AtTPC1, VfTPC1 represents a native two-pore channel variant that

activates faster and at more negative voltages, deactivates slower and is much less susceptible to blocking luminal Ca^{2+}.

Fabaceae and Brassiceae TPC1 channels are polymorphic in luminal Ca^{2+} sensing residues

To gain insights into the functional domains of these Brassicacea and Fabaceae TPC1 channel proteins underlying their different response to membrane voltage and luminal Ca^{2+}, we aligned not only the AtTPC1 and VfTPC1 but also other TPC1-like amino acid sequences of these plant families. The overall amino acid sequence comparison revealed the typical TPC1 characteristics like the tandem Shaker motif, the canonical cytoplasmic EF hands and the non-canonical luminal Ca^{2+} sensor. When we inspected the alignment for polymorphic functional TPC1 channel sites, we focused on charged residues in regions that are involved in luminal Ca^{2+} coordination and sensitivity in AtTPC1, namely the luminal Ca^{2+} sensor sites 1 and 2 (Asp240/Asp454/Glu528, Glu239/Asp240/Glu457, respectively) and the luminal pore mouth region (site 3) (Fig. S5a; Dadacz-Narloch et al., 2011; Kintzer and Stroud, 2016; Dickinson et al., 2022). We found that these sites were highly conserved among the Brassicacea channels. Only two of the 12 TPC1 variants tested (BrTPC1, LeTPC1) exhibit a neutralizing substitution at sites homologous to the AtTPC1 pore mouth residue Asp606. In contrast, most TPC1-types of the Fabaceae species show one up to three non-conservative variations of the residues. First, 11 of the 14 Fabaceae TPC1 channels harbor a non-charged asparagine or glutamine instead of the negatively charged glutamate at sites homologous to AtTPC1-Glu456 or -Glu457 (Fig. S5a). Second, remarkably, this E456Q/E457N polymorphism was additionally accompanied by the neutralization of one or two negatively charged residues within the luminal pore mouth in all Fabaceae TPC1 channels, with the exception of *Bauhinia tomentosa* BtTPC1 (site 3, Fig. S1a). In this regard, the Fabaceae TPC1 channels group in two clusters, containing either one or two non-charged residues (Ala/Val, Asn) at the homologous sites to AtTPC1-Glu605 and -Asp606 (Fig. S5b). The faba bean TPC1 channel now belongs to the subgroup with the hallmark triple polymorphism and contains alanine and asparagines at sites homologous to AtTPC1-Glu457/Glu605/Asp606, such as Asn458, Ala607 and Asn608 (Fig. S5a).

Polymorphic AtTPC1 triple mutant mimics the unique VfTPC1 channel features

In order to clarify whether these three polymorphic sites are responsible for the different gating behavior of the two TPC1 channel types, a series of site-directed mutagenesis was initiated in AtTPC1. This resulted in the GFP-marked double and triple AtTPC1 mutants E605A/D606N and E457N/E605A/D606N. When transiently expressed in the background of the TPC1-loss-of-function mutant *tpc1-2*, both the double and triple mutants were properly targeted to the vacuole membrane (Fig. S1) and gave rise to the typical SV/TPC1 channel currents upon depolarization (Fig. 1a). In the absence of luminal Ca^{2+}, the current voltage curves ($I_{ss}/C_m(V)$) and even more so the activation voltage curves ($G/G_{max}(V)$) of the double and triple mutants appeared shifted to more negative voltages by about 30 mV compared to wild type AtTPC1 (Fig. 1b, 2a, S4b). The changed voltage dependence of these AtTPC1 mutants was reflected in V_1 and V_2 values similar to wild type VfTPC1 (Fig. 2b). When the two mutants faced 10 mM luminal Ca^{2+}, again the current and activation voltage curves as well as the V_1, V_2 values resembled those of VfTPC1 (Figs. 1b, 2). This indicates that the E605A/D606N exchange is already sufficient to provide AtTPC1 with the voltage and Ca^{2+} sensitivity of VfTPC1. An additional D457N replacement did not further support the transition from an Arabidopsis into a hyperactive TPC1 channel. The fact that AtTPC1 channels carrying the VfTPC1 polymorphisms (i.e. double or triple residue substitutions) exhibit a low luminal Ca^{2+} susceptibility is best displayed by the channel behavior to 50 mM Ca^{2+}. Under such high luminal Ca^{2+} loads, almost no SV/TPC1 currents were observed with wild type AtTPC1 (Fig. 1). The current and activation voltage curves ($I_{ss}/C_m(V)$, $G/G_{max}(V)$) of the AtTPC1 double/triple mutants (E605A/D606N, E457N/E605A/D606N) and VfTPC1, however, demonstrate a continued similar strong TPC1 channel activity even at this extreme luminal Ca^{2+} level (Fig. 1b, 2).

<u>3D topology of VfTPC1 and AtTPC1 triple mutant mimics that of *fou2*</u>

In an attempt to determine the structural basis for the functional differences between *V. faba* and *A. thaliana* TPC1, we aimed to determine the cryoEM structure of VfTPC1, expressed and purified by similar conditions to that of AtTPC1 (Dickinson et al., 2022). Surprisingly, the biochemical behavior of VfTPC1 was significantly different than that of AtTPC1 and we were unable to recover any usable material after purification. Instead, we constructed a homology model of VfTPC1 using our high resolution cryoEM structure of Ca^{2+}-bound AtTPC1 D454N as a template. From our previous

structures of wild-type AtTPC1 and *fou2* (Kintzer and Stroud, 2016; Dickinson et al., 2022), we determined that the pore mouth operates a luminal, inhibitory Ca^{2+} sensor that is coupled to the functional voltage sensing domain (VSD2). In the wild-type and *fou2* structures, the pore mouth contains acidic residues (Glu605, Asp606 and Asp607) that line the conduction pathway above the selectivity filter. In the wild-type crystal structure, Glu605 binds a divalent metal on the symmetry axis. In our high-resolution structure of *fou2* (Dickinson et al., 2022), we showed that these residues rearrange to interact with the hydration shell around a bound metal in the selectivity filter and that Asp606 in *fou2* moves to the position of Glu605 in the wild-type structure, suggesting that both acidic residues regulate channel function. In our homology model of VfTPC1, neutralization of pore mouth acidic residues (A607 and N608, equivalent to E605 and D606 in AtTPC1) clearly alters the electrostatics of the pore. These substitutions almost certainly prevent the pore mouth from binding the inhibitory Ca^{2+} observed in the wild-type structure (Fig. 3a), and from interacting with the water network in the pore as seen in *fou2* (Dickinson et al., 2022). While the alleviation of inhibitory Ca^{2+} binding has a clear functional consequence, the effects of altering pore hydration is less obvious. It is possible that the pore mouth operates a “secondary” selectivity filter or gates the entrance of ions into the primary selectivity filter. In addition to perturbations in the pore mouth, VfTPC1 also contains an amino acid substitution (Asn458) in the inhibitory Ca^{2+} binding site located on the luminal side of VSD2 (Fig. 3b). This Ca^{2+} site has been previously shown to attenuate voltage-dependent activation by “stapling” the resting state VSD to the pore (Dickinson et al., 2022). In VfTPC1, Glu457 has been replaced with a neutral asparagine (Asn458) and is probably unable to participate in Ca^{2+} chelation, thus lowering the affinity of the site for luminal Ca^{2+}.

<u>Pore residues Glu605 and Asp606 do not influence either cation permeability or the single channel conductance of AtTPC1</u>

Due to the relatively close location of the pore residues Glu605 and Asp606 to the selectivity filter (Fig. 3; Kintzer et al., 2018), we investigated their influence on the cation permeability of TPC1 in patch clamp experiments with TPC1-overexpressing HEK cells under bi-ionic cation conditions (Fig. S6). With Na^+ on the cytosolic side of the membrane (i.e. in the pipette medium), Na^+ ions (150 mM) could be readily exchanged for the same or ten-fold lower concentration of K^+ or Ca^{2+}, respectively, on the extracellular side of the membrane by perfusion of the bath medium. Under these

experimental conditions the bath medium mimicked the vacuolar lumen. However, at 15 mM Ca^{2+} facing the extracellular/luminal side of the TPC1 channel protein, the activity of AtTPC1 wild type channel should be mostly suppressed, but not that of VfTPC1 and the AtTPC1 double mutant E605A/D606A (Fig. 1). To still allow current measurements for AtTPC1 channels with wild-type pore region under external high Ca^{2+}-based solute conditions, the AtTPC1 channel variant D240A/D454A/E528A (Guo et al., 2017) with damaged luminal Ca^{2+} sensing site 1 was additionally used. Under the various external cation (Na^+, K^+, Ca^{2+}) conditions, the TPC1 outward currents were pre-activated by a voltage pulse from -70 mV to +100 mV, to subsequently record current relaxation under deactivating voltage pulses (Fig. S6b-e). Based on the TPC1 outward/inward current relaxation, the reversal potentials were determined and used to calculate the relative permeability ratios of K^+ or Ca^{2+} to Na^+. We found that neutralizing luminal Ca^{2+} coordination at site 1 (D240A/D454A/E528A; Guo et al., 2017) or in the pore (E605A/D606A) did not alter the weak ability of the AtTPC1 wild type channel to discriminate between the permeating Na^+ and K^+ ions (Table S2). However, VfTPC1 and the AtTPC1 channel variants differed significantly in their preference for these physiological relevant monovalent cations. While VfTPC1 was slightly more permeable to K^+ than to Na^+, the opposite was true for all AtTPC1 channel variants. Therefore, this difference in the Na^+/K^+ selectivity is not related to the pore residues Glu605 and Asp606. In comparison, a relative permeability ratio P_{Ca}/P_{Na} of about 5.5 and 6 was derived for the AtTPC1 mutants and VfTPC1, respectively, suggesting a higher selectivity for Ca^{2+} over Na^+ for these channels. Thus, even though the pore residues Glu605 and Asp606 mediate luminal Ca^{2+} inhibition, they do not influence the Ca^{2+} permeability of the TPC1 channel.

A negative charge ring at the pore entrance promotes the single channel conductance of BK channels (Brelidze et al., 2003). To examine whether the negatively charged residues at the luminal pore entrance of AtTPC1 may play a similar role, single channel currents were recorded at different positive membrane voltages (Fig. S7a). Under symmetrical K^+ conditions (100 mM) a single channel conductance of about 80 pS was determined for AtTPC1 wild type (Fig. S7b, c). With respect to the dimeric structure of TPC1, the neutralizations in the AtTPC1 double mutant E605A/D606A results in the removal of a total of four negative charges in the luminal pore vestibule. Nevertheless, the unitary conductance of the mutant was unchanged. Moreover, VfTPC1 has a threefold higher unitary conductance than AtTPC1 (250 pS, Fig. S7; cf. Schulz-

Lessdorf and Hedrich, 1995), despite its neutral luminal pore residues at the homologous sites to AtTPC1. These facts indicate that these luminal polymorphic pore residues (Glu605, Asp606 in AtTPC1) apparently do not contribute to the conductance of TPC1.

Hyperexcitability of vacuoles equipped with VfTPC1 and AtTPC1 triple mutant

The hyperactivity of the AtTPC1 channel mutant *fou2* leads to a hyperexcitability of the vacuole (Jaslan et al., 2019). Since VfTPC1 wild type and the AtTPC1 pore mutants exhibit *fou2*-like hyperactive channel characteristics (Figs. 1, 2), we tested their effect on vacuole excitability. For this, we conducted current-clamp experiments in the whole-vacuole configuration (Jaslan et al., 2019) with vacuoles released from mesophyll protoplasts transiently transformed with either VfTPC1, AtTPC1 wild type or the triple AtTPC1 mutant E457N/E605A/D606N. To mimic more physiological luminal Ca^{2+} conditions (see for review Schönknecht, 2013, and references therein), the electrical polarization of the vacuole membrane was measured in the presence of 0.2 mM luminal Ca^{2+}. For TPC1-dependent vacuolar excitation, depolarizing current pulses of increasing amplitudes in the range of 10 to 1000 pA were temporarily injected from a resting voltage of -60 mV. The vacuole membrane responded to the current stimulus with a highly depolarized voltage peak which quickly relaxed to a less depolarized voltage plateau that persisted until the end of the stimulation phase (Fig. 4, S8a). Thereby, both the voltage peak and in particular the voltage stimulus-plateau appeared more depolarized with AtTPC1 wild-type channels than with the AtTPC1 triple mutant and the VfTPC1 wild-type channels (Fig. S8b, c). After current stimulus, the vacuole membrane equipped with VfTPC1 channels remained depolarized at a voltage of about 0 mV (i.e. at the equilibrium potential for K^+) during the entire subsequent recording period of 10 s, regardless of the stimulus intensity (Fig. 4, Table S1). In contrast, when AtTPC1-equipped vacuoles were challenged with even the highest current stimulus (1 nA), the post-stimulus voltage remained depolarized for only a short period ($t_{plateau}$ ~ 0.4 s, Table S1) before relaxation to the resting voltage occurred. In comparison to AtTPC1 wild type, the presence of the AtTPC1 triple mutant in the vacuole membrane strongly prolonged the lifetime of the depolarized post-stimulus voltage-plateau phase at all current stimuli (Fig. 4, Table S1). Except of one vacuole, all other five AtTPC1-triple mutant vacuoles already responded to the lowest current pulses such as 10, 30 or 70 pA with sustained post-stimulus depolarization over the entire recording period.

In other words, AtTPC1-triple mutant vacuoles were also hyperexcitable, behaving very much like the VfTPC1 vacuoles. This indicates that the hyperexcitability of vacuoles harboring the AtTPC1 triple mutant or the VfTPC1 channels correlates with their shifted voltage activation threshold (Fig. 4, S8).

Voltage activation threshold of TPC1 determines vacuole excitability

To analyze the dependency of the tonoplast excitability on the activation threshold of TPC1 in depth, we performed computational cell biology experiments. In a previous study we have presented a computational model that allows to simulate very precisely the phenomenon of TPC1-mediated vacuole excitability (Jaslan et al. 2019). We applied this model now with different TPC1 activation thresholds (Fig. 5a). At standard conditions (Fig. 5, blue) a current stimulus induced a vacuolar excitation with its characteristic phases (Fig. S6a), with the duration of the final plateau phase depending on the stimulus strength (Fig. 5c). If now the TPC1 activation curve was shifted slightly to more negative voltages (Fig. 5a, black), the vacuole membrane remained in the excited state after stimulation (Fig. 5b, black) as it was observed in the case of vacuoles acting with VfTPC1 or the AtTPC1 triple mutant (Fig. 4). If the activation threshold of TPC1 was shifted to more positive voltages (Fig. 5a, pink), the duration of the excited state and therefore the duration of the plateau phase decreased (Fig. 5b, d). While the vacuole membrane still responded to the stimulus intensity in an almost linear manner, the response was less pronounced when the activation threshold was shifted positive (Fig. 5e). Thus, the sensitivity of the vacuole membrane can be adjusted by regulating the voltage activation threshold of TPC1.

Discussion

In this study we identified polymorphic differences in luminal Ca^{2+} coordination sites of native TPC1-like channels from different plant species. In particular, we compared VfTPC1 from *Vicia faba* and AtTPC1 from *Arabidopsis thaliana*, which differ by three functional residues, with one residue being part of the known luminal Ca^{2+} sensor site 2 and two other residues within the luminal pore mouth region, forming the new luminal Ca^{2+} sensor site 3. In comparison to AtTPC1, VfTPC1 is hyperactive and less sensitive towards luminal Ca^{2+}.

<u>Impaired pore Ca^{2+} sensor confers hyperactivity to the native *Vicia faba* TPC1 channel</u>

Of the three luminal Ca^{2+} sensor sites identified so far in AtTPC1 channel (Figs. 1, 2; Dadacz-Narloch et al. 2011, Guo et al. 2016, Kintzer and Stroud 2016, Dickinson et al. 2021), only Glu457/458 from site 2 and the two pore residues Glu605 and Asp606 from site 3 are polymorphic (Fig. S5a). In contrast to AtTPC1, VfTPC1 harbors neutral residues at all three homologous polymorphic sites (Asn458, Ala607, Asn608). Due to the altered voltage dependency and reduced susceptibility to blocking luminal Ca^{2+}, the native VfTPC1 channel exhibited hyperactive channel features (Figs. 1-3, S4), thereby conferring hyperexcitability to the vacuole, as did the artificial *fou2* channel (Fig. 3; Jaslan et al. 2020).

Dadacz-Narloch and co-authors has previously shown that neutralization of the residue Glu457 to Asn or Gln in AtTPC1 alone was sufficient to decrease the luminal Ca^{2+} sensitivity of the corresponding single mutant channels E457N/Q (Dadacz-Narloch et al., 2011) as here with the pore mutant E605A/D606N (Fig. 2). However, voltage-dependent activation of these E457N/Q mutants was shifted to positive voltages while that of the pore mutant E605A/D606N to negative voltages. In other words, channel closing was promoted in the AtTPC1 mutants E457N/Q (Dadacz-Narloch et al., 2011) but channel opening in the pore mutant E605A/D606N (Fig. 2). Interestingly, the promoting effect of the double pore mutation on channel gating was not attenuated by the additional mutation E457N in the E457N/E605A/D606N triple mutant (Fig. 2). This suggest that the pore Ca^{2+} sensor site is dominant and can override the opposite effect of residue Glu457 on voltage activation, leading to almost the same excitability of the vacuoles equipped with E457N/E605A/D606N triple mutant as with VfTPC1 (Fig. 4).

<u>Secondary Ca^{2+} sensing gate in the luminal pore entrance</u>

Early on, the acidic residues Glu605 and Asp606 that we pinpointed here were resolved in the crystal structure of AtTPC1 as constriction site within the cation conduction pathway (Kintzer and Stroud, 2016). These residues together with the neighboring Asp607 are located above the selectivity filter close to the luminal pore entrance. Recently, we showed that the luminal Ca^{2+} inhibition of AtTPC1 was strongly attenuated when all three of these residues are neutralized (E/D → Q/N) rather than exchanging individual residues only (Dickinson et al., 2022). Here, we have now demonstrated that the double mutation of Glu605 and Asp606 (E605A/D606N) in AtTPC1 is already sufficient to similarly impair the luminal Ca^{2+} sensitivity (Figs. 1, 2). In addition, these two residues influence voltage sensing both alone and together, leading to hyperactive *fou2*-like AtTPC1 channels with voltage-dependent activation thresholds close to the resting voltage of the vacuole membrane (Figs. 1, 2; Dickinson et al., 2022). Remarkably, the high-resolution cryoEM structures of the Ca^{2+}-insensitive TPC1 channel mutant *fou2* with damaged luminal Ca^{2+} binding site 1 show that the pore residue Asp605 is no longer directed to the conduction pathway (Dickinson et al., 2022). Thus, due to allosteric coupling to the voltage sensor, these pore residues Glu605 and Asp606 appear to form a secondary Ca^{2+} sensing gate within the ion transport pathway. Recent molecular dynamics simulations (Navarro-Retamal et al., 2021) indicated that the E605/D606 motif is very flexible and adapts to the direction of ion flow. During influx simulations, this motif moved towards the channel pore and eased the translocation of K^+ ions from the lumen toward the selectivity filter, while during efflux simulations it moved away and facilitated K^+ ions to exit the channel towards the lumen. This flow-dependent flexibility in combination with the allosteric coupling to the voltage sensor may suggest the E605/D606 motif to be an important player in a valve-like regulatory mechanism. The efflux from the cytosol to the lumen stabilizes the position found in the hyperactive *fou2* mutant, which may suggest that ion efflux stabilizes the open channel. In contrast, the influx from the lumen to the cytosol drives the valve towards the pore, which may have the opposite effect and closes the channel. In such a context, the neutralizing E605A/D606N mutations would reduce the electrostatic interactions between the E605/D606-motif and the permeating ions, and would, as observed, result in channels that open with less activation energy.

<u>Uncoupling pore Ca^{2+} coordination from gating via the E605/D606-motif</u>

The formerly proposed mechanism provides a straightforward explanation for the reduced voltage activation threshold of VfTPC1 and both AtTPC1-E605A/D606N mutants in the absence of luminal Ca^{2+}. However, it does not yet explain the reduced Ca^{2+} sensitivity of these channels. To understand this phenomenon, it is necessary to have a closer look at the pore of TPC1-like channels. The recent MD simulations of the pore of AtTPC1 did not only reveal the structural flexibility of the E605/D606-motif but also pointed to a Ca^{2+} coordination site (D269/E637) close to the luminal entrance of the selectivity filter. Interestingly, the same residues were identified in an independent computational docking approach as binding site for spermine (Pottosin et al., 2020). In VfTPC1 these residues correspond to D271/E639. Ca^{2+} coordination in the pore, in combination with the E605/D606-motif, may add another level of Ca^{2+} regulation to the gating process. Higher luminal Ca^{2+} increases the probability of Ca^{2+} to occupy the D269/E637 coordination site in the pore and may stabilize the E605/D606-motif in the pore-facing conformation by electrostatic interactions. As mentioned above, this is accompanied by greater energy needed to activate the channel. Also here, the neutralization by the mutations E605A/D606N would uncouple pore Ca^{2+} coordination from gating.

Voltage activation threshold of TPC1 controls vacuole excitability and plant performance

AtTPC1 and VfTPC1 differ in their voltage activation threshold, with that of VfTPC1 being closer to the vacuole resting membrane voltage than that of AtTPC1 (Fig. 2). The voltage activation threshold of the TPC1 channel variant has a strong influence on the strength of vacuole excitability (Fig. 4, 5, S8). Therefore, to trigger vacuole excitability with AtTPC1 wild type channels, channel function must be modulated such that the voltage activation threshold shifts near to the vacuole resting membrane voltage, opening a sufficient number of TPC1 channels. Conversely, hyperactive TPC1 channels like VfTPC1 must be kept under control in their natural environment to avoid permanent vacuolar excitation and thus retarded plant growth through activation of jasmonate-associated wounding responses (cf. *fou2*, Bonaventure et al., 2007b; Lenglet et al., 2017). This would require reducing or enhancing the effect of inhibitory or stimulatory regulators on voltage gating. When AtTPC1 was expressed in an animal expression system instead its natural plant environment, channel gating was strongly shifted to negative voltages (Guo et al., 2016). This and other observations additionally

suggest that post-translational modification of TPC1 and/or interaction with regulatory proteins (e.g. kinase, phosphatase, 14-3-3 proteins), lipid compounds/derivatives or cations contribute to the modulation of TPC1 channel gating in planta (Hedrich and Neher, 1987; Allen and Sanders, 1995; Schulz-Lessdorf and Hedrich, 1995; Bethke and Russell, 1997; Pei et al., 1999; Carpaneto et al., 2001; Pottosin et al., 2005; Latz et al., 2007; Perez et al., 2008; Schulze et al., 2011; Gutla et al., 2012).

The luminal Ca^{2+} concentration regulates the ion flux through TPC1 by various paths that apparently show some variability among different species. However, in the rough tendency this effect is the same in all cases: more Ca^{2+} in the vacuole desensitizes the channel. TPC1-triggered vacuole excitation, in turn, can cause the release of Ca^{2+} from the vacuole to the cytosol via a Ca^{2+} homeostat with a striking correlation between the duration of excitation and the released Ca^{2+} (Dindas et al., 2021). Here, we show now that the voltage activation threshold of TPC1 has a direct influence on the excitation time of the vacuolar membrane (Fig. 3, 4, S6e). Luminal Ca^{2+} has therefore a dual role in excitation-induced vacuolar Ca^{2+} release. In comparison to a smaller luminal Ca^{2+} concentration, a higher luminal Ca^{2+} concentration means a larger transmembrane Ca^{2+} gradient which would also mean a larger Ca^{2+} release if the Ca^{2+} homeostat is always stimulated to the same degree. A Ca^{2+} tuning of TPC1 has the potential to dampen or even equilibrate the effect of the larger gradient. A higher luminal Ca^{2+} concentration downregulates the TPC1 activity, which in turn reduces the excitation time and results in a shorter Ca^{2+} release of larger amplitude.

Acknowledgements

The work was supported by DFG Koselleck to R.H., a doctoral fellowship from the China Scholarship Council (CSC) and a STIPET fellowship from the German Academic Exchange Service (DAAD) to J.L., the CONICYT-FONDEQUIP project EQM160063 to I.D. and C.N.-R., a Fondecyt-Enlace project of the Universidad de Talca to I.D., and the postdoc grant FONDECYT no. 3170434 of the Comisión Nacional Científica y Tecnológica of Chile to C.N.-R. We are grateful to Parathy Yogendran for transient transfection of HEK293 cells. We would like to thank Matthias Freund for his support in statistical analysis and Armando Carpaneto for discussion.

MATERIALS AND METHODS

Plant materials and growth conditions

The *Arabidopsis thaliana tpc1-2* mutant (Peiter et al., 2005) was grown in a growth chamber under short day conditions (8 h light, 16 h dark) with a day/night temperature regime of 22/16 °C, a photon flux density of 150 µmol m^{-2} s^{-1} and a relative humidity of about 60%. *Vicia faba* plants were grown in the greenhouse at a 16 h day/8 h dark photoperiod, a day/night temperature regime of 16/14°C and a light intensity of approximately 150 µmol m^{-2} s^{-1}.

RNA sequencing

Leaves from 6- to 8-week-old *Vicia faba* plants were harvested and mesophyll RNA was extracted using the NucleoSpin Plant RNA extraction kit (Macherey-Nagel, Düren, Germany) according to the manufacturer's instructions. For guard cell RNA extraction epidermal fragments were isolated using the blender method (Bauer et al., 2013). Total RNA from three individual biological replicates was prepared and subjected to RNA-sequencing on an Illumina NextSeq500 platform. High-quality RNA-seq paired-end reads were quality checked using FastQC (version 0.11.6) and transcriptomes were *de novo* assembled individually using Trinity (version 2.5.1 Release). Finally, the TRAPID pipeline was employed for processing of assembled transcriptome data including transcript annotation (Bucchini et al., 2020). Based on AtTPC1 homology, identical VfTPC1 transcripts were identified in mesophyll and guard cell fractions, and the obtained sequence information was used to clone the VfTPC1 CDS by a PCR-based approach. The *VfTPC1* mRNA sequence is deposited at Genbank under the following accession number: BankIt2410619 VfTPC1_mRNA MW380418.

Cloning and site-directed mutagenesis

After the total RNA was extracted from mature leaves of two-week-old *Vicia faba* plants and reverse transcribed into complementary DNA (cDNA), VfTPC1 was amplified from the cDNA library, essentially as described (Dadacz-Narloch et al., 2013). For patch clamp experiments with vacuoles, the cDNA coding sequences of the AtTPC1 and VfTPC1 channel variants were cloned into the modified pSAT6-eGFP-C1 vector (GenBank AY818377.1) and pSAT6-eYFP-C1 vector (GenBank DQ005469), respectively, using the uracil-excision-based cloning technique (Nour-Eldin et al., 2010), essentially as described by (Dadacz-Narloch et al., 2011). The resulting

AtTPC1-eGFP and VfTPC1-eYFP constructs were under the control of the 35S or ubiquitin promoter (UBQ10), respectively. For patch clamp experiments with HEK cells, the eYFP coding sequence (Nagai et al., 2002) was fused without the stop codon to the 5' end of the TPC1 cDNA coding sequences and then cloned together into the pcDNA3.1 vector (GenBank MN996867.1). In analogy to (Dadacz-Narloch et al., 2011), a modified USER fusion method was used to introduce site-directed mutations in the wild type AtTPC1 construct. The sequences of the primers used for subcloning and mutagenesis are listed in Table S2. All channel variants were tested for their sequences.

Transient protoplast transformation

Essentially following the protocols from (Sheen, 2002) and (Yoo et al., 2007), mesophyll protoplasts were released from 6- to 7-week-old *tpc1-2* Arabidopsis mutant plants and transiently transformed with the different TPC1 channel constructs. For channel expression, protoplasts were then stored in W5 solution (125 mM $CaCl_2$, 154 mM NaCl, 5 mM KCl, 5 mM glucose, 2 mM Mes/Tris, pH 5.6, 50 µg ml^{-1} ampicillin) at 23°C in the dark for usually two days.

HEK cell transfection

HEK293 cells were transfected with the respective eYFP-TPC1-fused constructs with lipofectamine2000 (ThermoFisher, Waltham, USA) according to the manufacturer's instructions. Cells were seeded 18-24 hours after transfection in glass coverslips (diameter 12 mm). Protein expression was verified on the single-cell level by the appearance of eYFP-fluorescence in the plasma membrane upon excitation with a 473 nm laser.

Subcellular targeting

Vacuolar membrane localization of the expressed eGFP/eYFP-fused TPC1 channels was verfied by imaging the fluorescence signal of transformed protoplasts and vacuoles with a confocal laser scanning microscope (TCS SP5, Leica, Mannheim, Germany) (Dadacz-Narloch et al., 2013). eGFP and eYFP were excited with an Argon laser at 490 and 514 nm, respectively, and the emission of fluorescence was monitored between 500 and 520 nm for eGFP and between 520–540 nm for eYFP. Red autofluorescence of chlorophyll was excited at 540 nm and acquired between 590 and

610 nm. For expression analysis in HEK293 cells, a confocal laser scanning microscope (SP700, Zeiss, Germany) equipped with three laser lines (488 nm: 10 mW, 555 nm: 10 mW, 639 nm: 5 mW) was used. Images were processed with ZEN software (ZEN 2012, Zeiss) or Fiji, Version ImageJ 1.50 (Schindelin et al., 2012).

Whole-vacuole patch clamp experiments

Vacuoles were released from protoplasts in the recording chamber two days after transformation using a vacuole release (VR) solution (Lagostena et al., 2017). The VR solution was modified and composed of 100 mM malic acid, 155 mM N-methyl-D-glucamine, 5 mM EGTA, 3 mM $MgCl_2$, 10 mM Hepes/Tris pH 7.5 and adjusted to 450 $mOsmol \cdot kg^{-1}$ with D-sorbitol. The whole vacuole configuration was then established with TPC1-transformed vacuoles which were easily identified upon their eGFP- or eYFP-based fluorescence measured between 510 and 535 nm after excitation at 480 nm with a *precisExcite HighPower* LED lamp (Visitron Systems GmbH, Puchheim, Germany). Patch pipettes were prepared from Harvard glass capillaries (Harvard glass capillaries GC150T-10, Harvard Apparatus, UK) and typically had a resistance in the range of 1.4-3.1 MΩ. The membrane capacitance (C_m) of the individual vacuoles accessed and compensated in patch clamp experiments ranged from 31.1 to 68.5 pF. Membrane currents and voltages were recorded with a sampling rate of 150 µs at a low pass filter frequency of 2.9 or 3 kHz using an EPC10 or EPC800 patch clamp amplifier, respectively (HEKA Electronic). Data were acquired with the software programs Pulse or Patchmaster (HEKA Electronic) and off-line analyzed with IGORPro (Wave Metrics).

Voltage recordings were carried out in the current-clamp mode as described (Jaslan et al., 2019). Briefly, after adjusting the membrane voltage to -60 mV by injection of an appropriate current, current pulses were applied in the range of 10 to 1000 pA for 200 ms. The duration of the post-stimulus depolarisation phase gives the time at which the initial depolarized voltage dropped by 50% to the holding voltage.

In voltage-clamp experiments macroscopic currents were recorded in response to 1-s-lasting voltage pulses in the range of -80 mV to +110 mV in 10 mV increments. The holding voltage was -60 mV. The corresponding current responses of each vacuole were analyzed with respect to the half-activation time ($t_{act\text{-}0.5}$) and steady-state current amplitudes (I_{ss}). The half-activation time ($t_{act\text{-}0.5}$) was the time at which 50% of the steady-state current amplitude was reached. As a normalization measure for the membrane surface of the individual vacuole, the determined steady state currents were

divided by the respective compensated membrane capacitance (C_m). Conductance/voltage curves ($G/G_{max}(V)$) were quantified from tail current experiments as a measure for the relative voltage-dependent open channel probability. Following pre-pulse voltages in the range of -80 to +110 mV, instantaneous tail currents were determined at -60 mV. According to Dickinson et al. (2020), the midpoint voltages (V_1, V_2) and the equivalent gating charges (z_1, z_2) were derived by fitting the $G/G_{max}(V)$ curves with a double Boltzmann equation (Dickinson et al. 2020). After pre-activation of TPC1 currents upon an instantaneous voltage pulse to either +80 mV or +100 mV, the current relaxation was recorded at voltages from -60 to 0 mV and the deactivation-half times ($t_{deact\text{-}0.5}$) were determined. The half-deactivation time ($t_{deact\text{-}0.5}$) denotes the time at which the initial tail current amplitude has declined by 50%.

In voltage-clamp experiments the standard bath solution facing the cytoplasmic side of the vacuole membrane contained 150 mM KCl, 1 mM $CaCl_2$, 10 mM Hepes (pH 7.5/Tris) and was adjusted with D-sorbitol to an osmolality of 520 mOsmol·kg^{-1}. The standard pipette solution at the luminal side of the tonoplast basically consisted of 150 mM KCl, 2 mM $MgCl_2$, 10 mM HEPES (pH 7.5/Tris) and was adjusted with D-sorbitol to a final osmolality 500 mOsmol·kg^{-1}. The pipette solution was supplemented with 10 mM or 50 mM $CaCl_2$ or adjusted to 0 mM Ca^2 by addition of 0.1 mM EGTA. In current-clamp experiments the standard bath medium additionally contained 2 mM $MgCl_2$ and the pipette solution was adjusted to 0.2 mM free Ca^{2+} by addition of 4.1 mM EGTA and 4.3 mM Ca^{2+} (https://somapp.ucdmc.ucdavis.edu/pharmacology/bers/maxchelator/webmaxc/webmaxcE.htm).

Patch clamp experiments with membrane patches

Vacuoles were isolated from transiently transformed protoplast by perfusion with a solution containing 10 mM EGTA, 10 mM Hepes/Tris pH 7,5, adjusted to 200 mosmol kg^{-1} with D-Sorbitol. Excised membrane patches with the cytosolic side of the tonoplast facing the bath medium were formed from the whole vacuole configuration. Single channel fluctuations were recorded with a sampling rate of 100 µs at a low pass filter frequency of 1 kHz using an EPC10 patch clamp amplifier. Single channel current amplitudes were determined from all-point histograms of the current recordings and plotted against the respective voltages. The single channel conductance for each membrane patch was derived from linear regression of the current-voltage plot. The bath medium contained 100 mM KCl, 0.5 mM $CaCl_2$, 10 mM Hepes (pH 7.5/Tris). The

pipette medium consisted of 100 mM KCl, 2 mM $MgCl_2$, 2 mM EGTA, 10 mM MES (pH 5.5/Tris). Both solutions were adjusted to 400 mosmol·kg^{-1} with sorbitol.

Patch clamp experiments with HEK cells

Whole-cell current recordings were performed at a setup described previously (Panzer et al., 2019). Data were acquired using Clampex 10.7 (Molecular devices, San Jose, USA) with 100 kHz sampling rate, low-pass filtered at 5 kHz, and analyzed with Clampfit 10.7 (Molecular devices) and OriginPro 2016 (Originlab, Northampton, USA). Pipette resistance (GB150F-8P, Scientific-Instruments, Hofheim, Germany) was 4-6 MΩ in standard bath solution. The standard pipette solution contained 150 mM NaCl, 2.5 mM $MgCl_2$, 0.3 mM free Ca^{2+} (adjusted by 4.3 mM $CaCl_2$ and 4 mM EGTA), 10 mM Hepes, (pH 7.4/Tris). The standard bath solution was composed of 150 mM NaCl, 10 mM HEPES, (pH 7.4/Tris). To determine the relative permeability ratio on the same HEK cell, the Na^+-based bath medium was replaced by either a K^+- or Ca^{2+}-based solution. The K^+-based bath medium contained 150 mM KCl, 10 mM HEPES, (pH 7.4/Tris), and the Ca^{2+}-based one consisted of 15 mM $CaCl_2$, 120 mM NMDG-Cl, 10 mM Hepes (pH 7.4/Tris).

For determination of the TPC1 ion selectivity, tail current experiments were conducted. After pre-activating the TPC1 channels by a voltage step from -70 mV (resting potential) to +100 mV for 500 to 1000 ms, the relaxation of the outward currents in response to hyperpolarizing voltage pulses was recorded either with 10 mV intervals reaching from +60 mV to -120 mV or in 5 mV decrements reaching from +30 mV to -40 mV to visualize and to analyze the reversal potentials, respectively. In order to clearly assign the reversal potential to TPC1 currents, which are not contaminated by leakage currents, the slope of the tail currents was determined and plotted against the corresponding voltages. The reversal potential for each solute condition was then determined by interpolation the smallest negative and positive slope values. The shift in the reversal potential $\triangle V_{rev}$ caused by the change of the external solution from either Na^+ to K^+ or Na^+ to Ca^{2+} solution was used to estimate the relative permeability ratios P_{Ca}/P_{Na} or P_K/P_{Na} essentially as described by (Sun et al., 1997). For calculation of the K^+ to Na^+ permeability ratio (P_K/P_{Na}) the following equation (1) was used (Hille, 1971):

$$\frac{P_K}{P_{Na}} = \frac{[K]}{[Na]} \cdot \exp\left(\frac{\Delta Vrev}{\alpha}\right) \quad (1)$$

where $\triangle V_{rev} = V_K - V_{Na}$, with the reversal potentials V_K and V_{Na} in K^+- or Na^+-based bath solution, respectively, and α= RT/F = 25.42 mV at 22°C. The relative permeability ratio P_{Ca}/P_{Na} was calculated using equation (2) derived from the extended Goldman-Hodgkin-Katz equation (Lewis, 1979):

$$\frac{P_{Ca}}{P_{Na}} = \frac{\left(1+\exp\left(\frac{V_{Ca}}{\alpha}\right)\right)\cdot\exp\left(\frac{\Delta Vrev}{\alpha}\right)\cdot[Na]}{4\cdot[Ca]} \quad (2)$$

where $\triangle V_{rev} = V_{Ca} - V_{Na}$ with the reversal potentials V_{Ca} and V_{Na} in Ca^{2+}- or Na^+-based bath solution, respectively, and α has same meaning as above.

Voltage convention in patch clamp experiments

The given membrane voltages refer to the cytosolic side of the vacuole membrane or HEK cell plasma membrane with zero potential on its luminal or extracellular side, respectively. In experiments with vacuoles performed in the presence of 50 mM luminal Ca^{2+} (Fig. 1, 2, S2d and S3d), the membrane voltages were corrected off-line by the corresponding liquid junction potential determined offline according to Neher (1992) and Ward and Schroeder (1994). Otherwise, no correction for the liquid junction potential was necessary.

Statistical analysis

Patch clamp experiments were conducted with individual vacuoles per each channel construct and solute condition. Due to a common data set, I_{ss}/C_m(V) and $G/G_{max}(V)$ curves for wild type AtTPC1 acquired under 0 and 10 mM luminal Ca^{2+} were identical to those shown in (Dickinson et al., 2022). Electrophysiological data are given as means ± SE or SD as indicated in the figure legends. The statistical analysis was performed using one-way-ANOVA followed by the Dunnett's or Tukey's posthoc comparison test. In order to test also the Ca^{2+}-induced shifts in the $V_{1/2}$ values for significant differences, the V_1 and V_2 mean values determined in the absence of luminal Ca^{2+} were subtracted from the individual V_1 and V_2 values, respectively, derived under 10 mM luminal Ca^{2+} conditions (Dickinson et al., 2022). In analogy, the Ca^{2+}-induced change in the $t_{act\text{-}0.5}$ values were analyzed for significant differences.

Statistical analysis was done with Origin 2020 (OriginLab, Northampton, Massachusetts, USA) and SPSS 2020 (IBM, New York, USA).

3D modelling

An atomic model of VfTPC1 was generated using the homology modelling program MODELLER B. (Webb and Sali, 2016), using the experimental AtTPC1 D454N (*fou2*) Ca^{2+}-bound structure (Dickinson et al., 2022) as a reference. The model was then relaxed into the 2.5 Å resolution *fou2*-Ca^{2+} map (Dickinson et al., 2022) using ISOLDE (Croll, 2018) and used for atomic interpretation.

In silico experiments

Electrical excitability of the vacuolar membrane was computationally simulated as described in detail before (Jaslan et al., 2019) involving a background conductance, voltage-independent K^+ channels of the TPK-type and the time- and voltage-dependent cation channel TPC1 that confers excitability to the vacuolar membrane. The delayed-activating behavior of the latter can be described mechanistically by four independent gates of two different types following the gating schemes $O_1 \leftrightarrow C_1$ and $O_2 \leftrightarrow C_2$ with the rate constants a_1, a_2, d_1, and d_2 for activation and deactivation, respectively: $a_1 = s^{-1} \times \exp[0.45 \times V \times F/(RT) - 0.26 \times \ln(\alpha)]$, $d_1 = s^{-1} \times \exp[-0.81 \times V \times F/(RT) + 0.26 \times \ln(\alpha) + 1.84]$, $a_2 = s^{-1} \times \exp[0.5 \times V \times F/(RT) - 0.26 \times \ln(\alpha) - 0.4]$, $d_2 = s^{-1} \times \exp[-0.5 \times V \times F/(RT) + 0.26 \times \ln(\alpha) + 3.0]$. To simulate TPC1s with different gating features, the parameter α has been set to 0.002, 0.01, and 0.05.

Figures

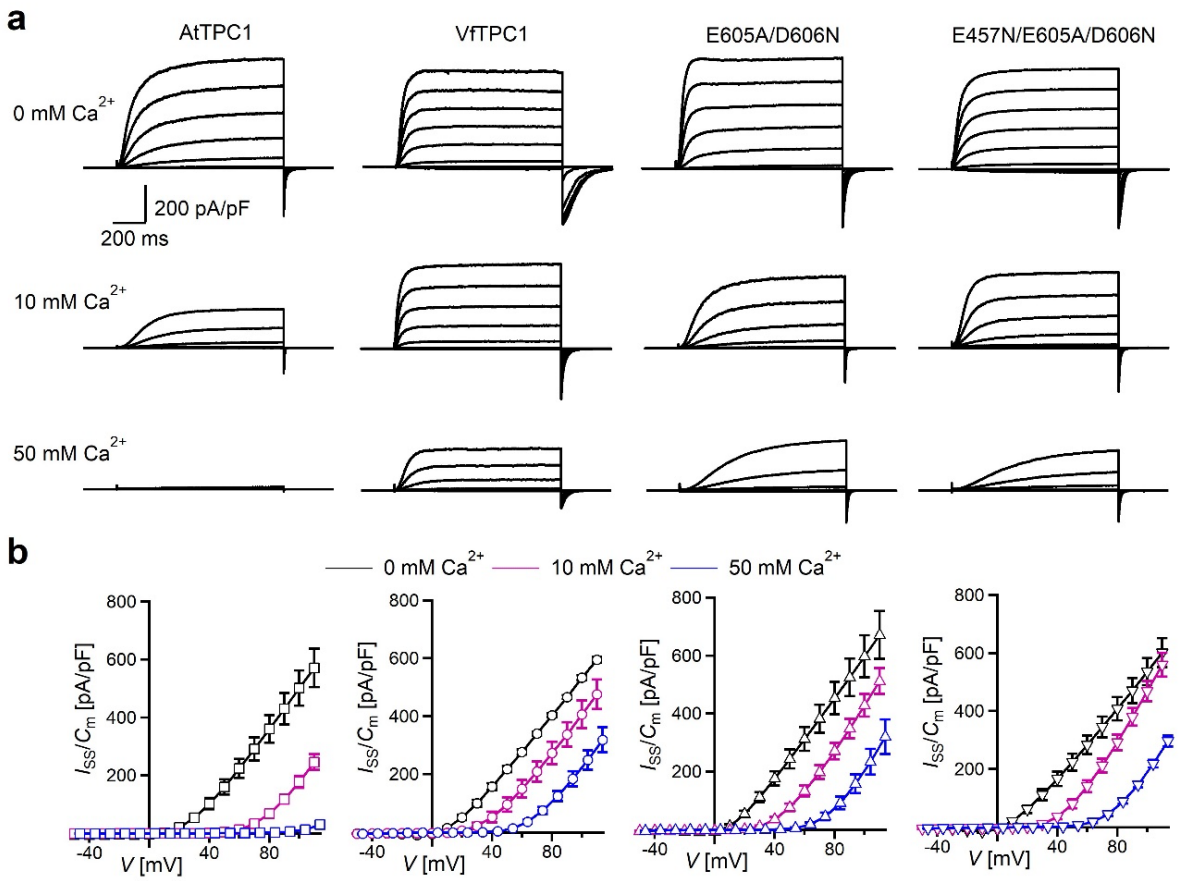

Fig. 1: Effect of voltage and luminal Ca^{2+} on TPC1/SV currents of *Vicia faba* and *Arabidopsis thaliana* channel variants.

a Macroscopic TPC1/SV current recordings from mesophyll vacuoles liberated from *Arabidopsis thaliana* protoplasts isolated from the TPC1-loss-of-function mutant *tpc1-2* and transformed with different TPC1 channel types. E605A/D606N and E457N/E605A/D606N represent AtTPC1 channel mutants. TPC1/SV currents elicited upon depolarizing voltages pulses in the range -80 mV to +110 mV in 20 mV increments at indicated luminal Ca^{2+} concentrations are shown.

b Normalized TPC1/SV currents (I_{ss}/C_m) derived from current recordings under different luminal Ca^{2+} conditions as those shown in (**a**) were plotted against the clamped membrane voltage (V). Symbols represent means ± SE. Squares = AtTPC1 wild type with $n_{0/10Ca}$ = 5, n_{50Ca} = 4; circles = VfTPC1 wild type with n_{0Ca} = 5, $n_{10/50Ca}$ = 6; upright triangles = AtTPC1-E605A/D606N with $n_{0/10Ca}$ = 5, n_{50Ca} = 4; reversed triangles = AtTPC1-E457N/E605A/D606N with $n_{0/10Ca}$ = 5, n_{50Ca} = 4. AtTPC1 wild-type data at 0 and 10 mM Ca^{2+} are identical to those shown in Dickinson et al. (2022).

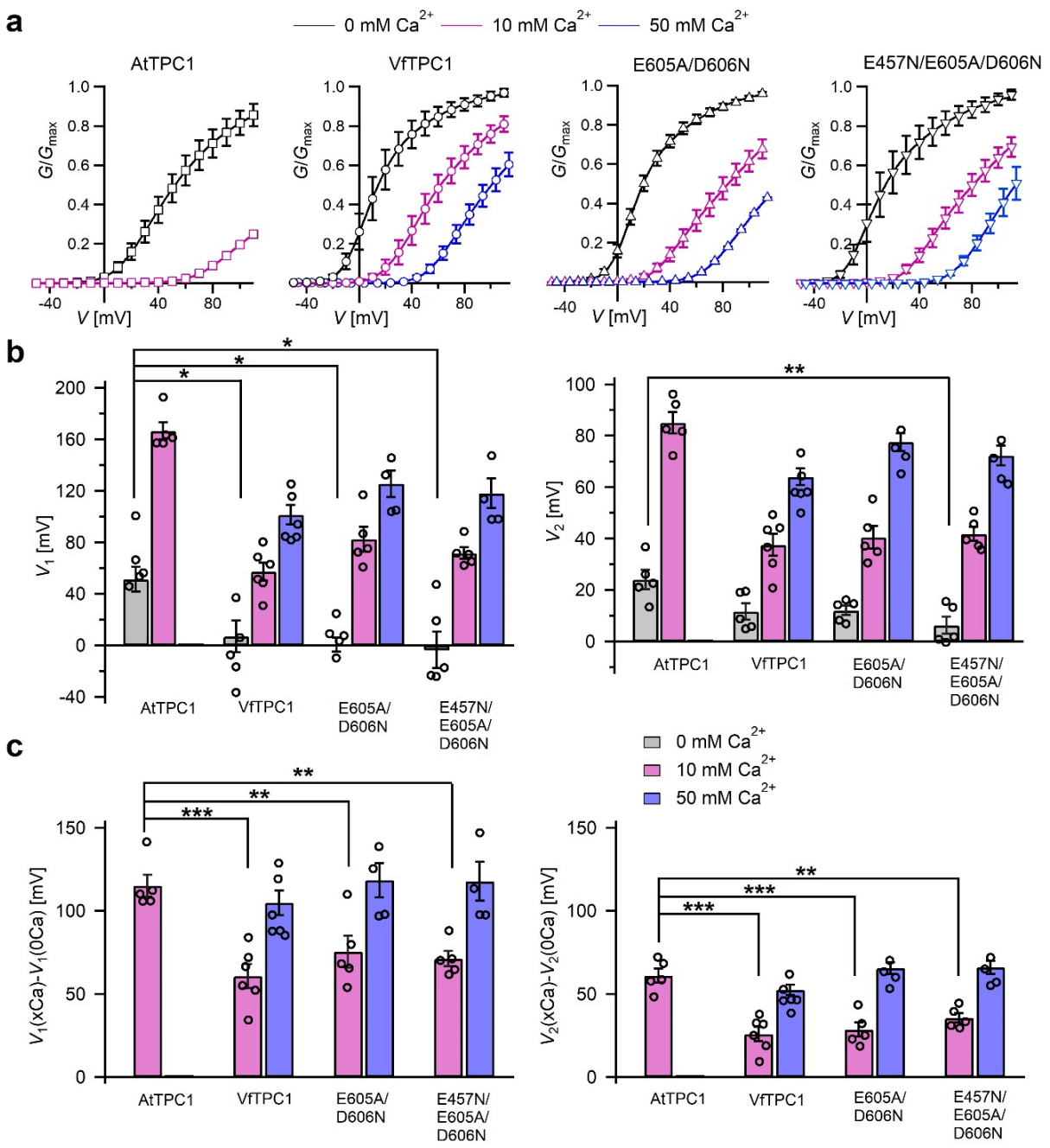

Fig. 2: Channel activity of *Vicia faba* and *Arabidopsis thaliana* TPC1 channel variants in response to membrane voltage and luminal Ca^{2+}.

a Normalized conductance-voltage plots (G/G_{max} (V)) determined for the different TPC1 channel variants as a measure for their relative open-channel probability under indicated luminal Ca^{2+} conditions. Best fits of the G/V plots to a double Boltzmann function are given by the solid lines. Squares = AtTPC1 wild type, circles = VfTPC1 wild type, upright triangles = AtTPC1-E605A/D606N, reversed triangles = AtTPC1-E457N/E605A/D606N.

b The midpoint voltages V_1 (left) and V_2 (right) derived from the fits of the *G*/*V* plots shown in (**a**) are given for the different channel variants at the indicated Ca^{2+} condition. To test for significant differences between the $V_{1/2}$ values under 0 mM luminal Ca^{2+}, a statistical analysis was performed with one-way ANOVA combined with a Dunnett's post hoc comparison test (*$p < 0.05$, **$p < 0.01$).

c The differences in the midpoint voltages V_1 (left) and V_2 (right) shown in (**b**) between 0 and 10 and if available between 0 and 50 luminal Ca^{2+} are shown. The changes in $V_{1/2}$ values related to a rise from 0 to at 10 Ca^{2+} were statistically analyzed with one-way ANOVA together with a Dunnett's post hoc comparison test (**$p < 0.01$; ***$p < 0.001$).

In **b, c** individual data points were inserted as open black circles into the bar chart. In **a-c** the number of experiments (n) was as follows: AtTPC1 wild type $n_{0/10Ca} = 5$; VfTPC1 wild type with $n_{0Ca} = 5$, $n_{10/50Ca} = 6$; AtTPC1-E605A/D606N $n_{0/10Ca} = 5$, $n_{50Ca} = 4$; AtTPC1-E457N/E605A/D606N $n_{0/10Ca} = 5$, $n_{50Ca} = 4$.

Data in **a-c** represent means ± SE. AtTPC1 wild-type data at 0 and 10 mM Ca^{2+} are identical to those shown in Dickinson et al. (2022).

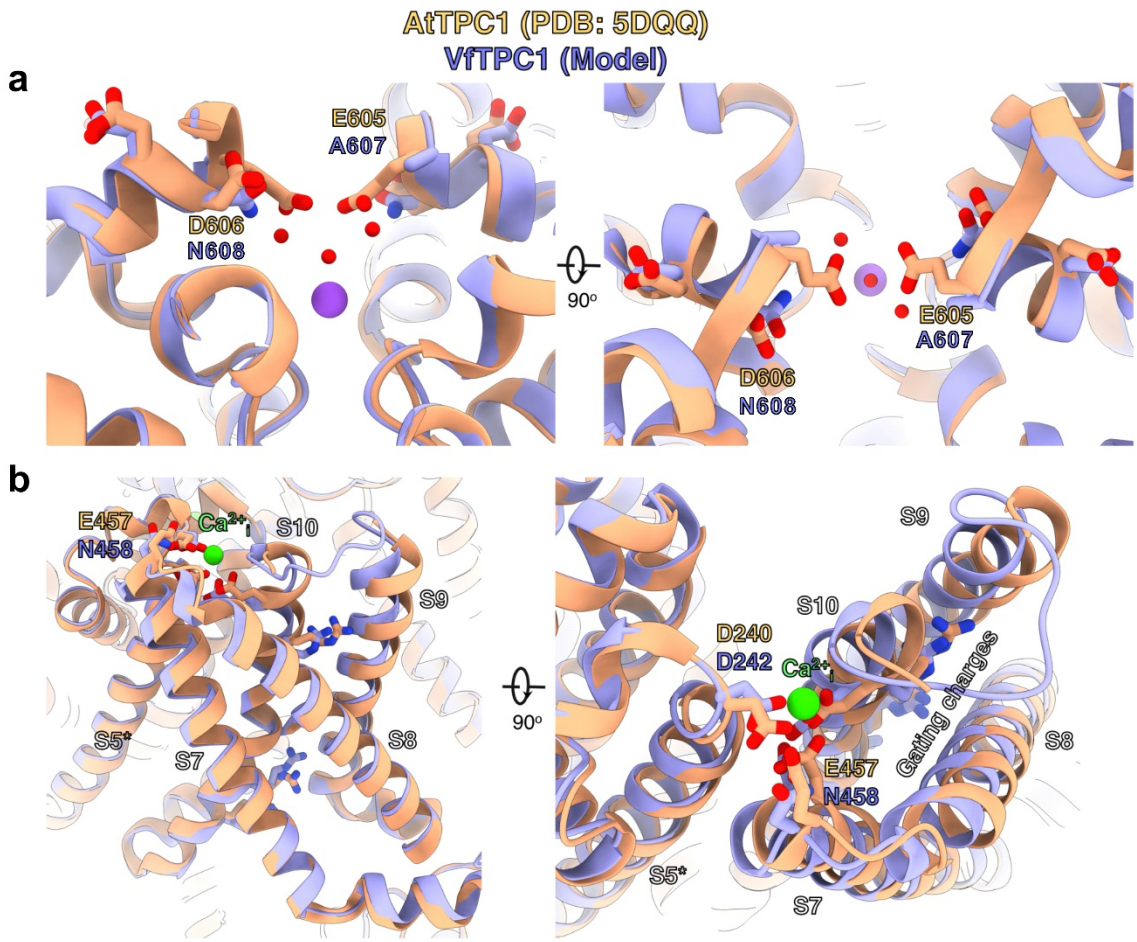

Fig. 3: Structural comparison between wild type AtTPC1 and a VfTPC1 homology model depicts functional consequences of sequence divergence.

a Orthogonal views of the pore mouth residues. The central purple and red spheres are Na^+ and waters, respectively, as observed in the cryoEM structure of *fou2* (Dickinson et al. 2022).

b Orthogonal views of the luminal Ca^{2+}-binding site on VSD2. For all panels, AtTPC1 is beige and VfTPC1 purple.

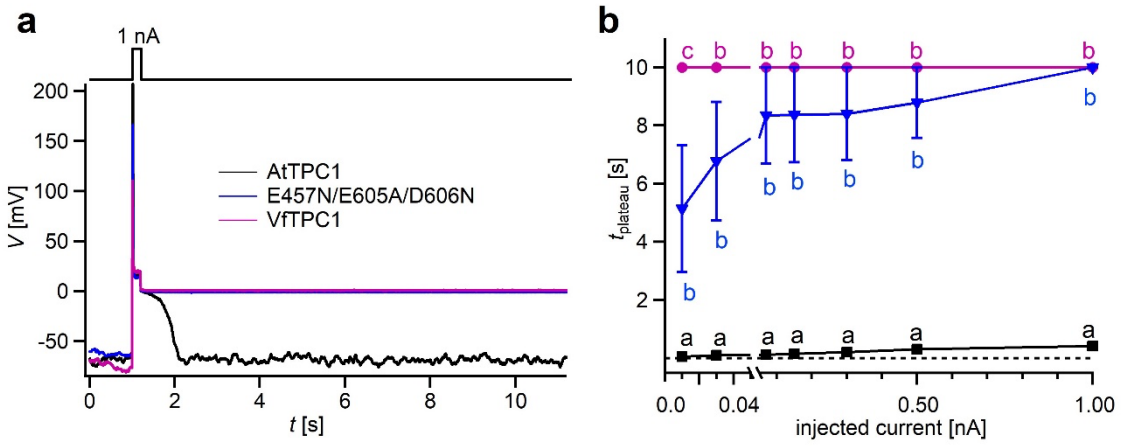

Fig. 4: Dependency of vacuole excitability on TPC1 channel variants.

a Superimposed voltage responses (lower panel) of individual vacuoles equipped either with VfTPC1 wild type (magenta), AtTPC1 wild type (black) or AtTPC1-triple mutant E457N/E605A/D606N (blue) to current injection of 1 nA (upper panel).

b Lifetime of the post-stimulus depolarization phase plotted against the corresponding injected current pulse. Symbols represent means ± SE (squares = AtTPC1 wild type; circles = VfTPC1 wild type; reversed triangles = AtTPC1-E457/E605A/D606N). Individual data points are listed in Table S1. Number of experiments for each channel type was n = 6. Significant differences between the channel variants are indicated by different letters (one-way ANOVA followed by a Tukey's post hoc comparison test). All experiments were carried out at 0.2 mM luminal Ca^{2+}.

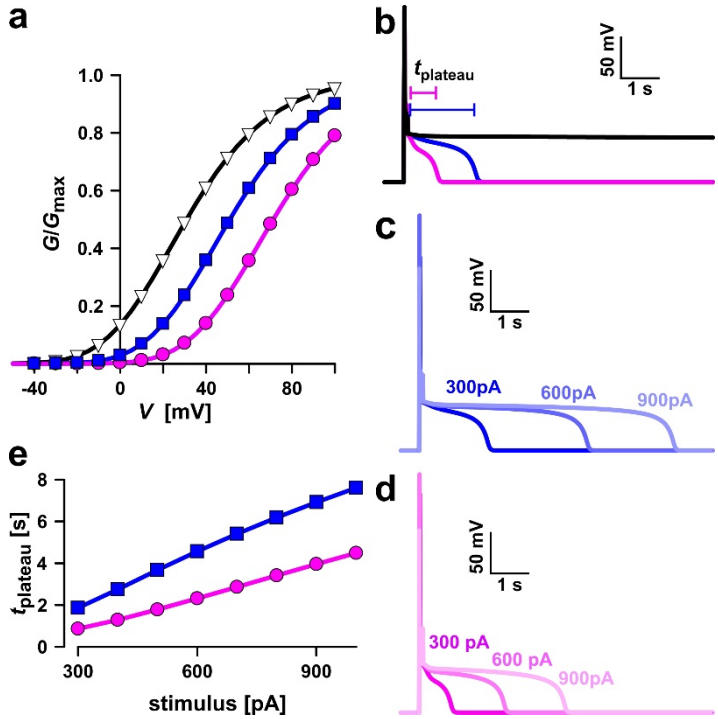

Fig. 5: Simulation of vacuolar electrical excitability with three different TPC1 variants.

a Gating characteristics (G/G_{max}) of three different TPC1-type channels.

b Simulation of vacuolar electrical excitability with the different TPC1 variants. Excitation was induced by a 300 pA pulse of 100 ms duration.

c Overlay of the electrical response of the vacuole having the blue-type TPC1 to 100 ms pulses of 300 pA, 600 pA and 900 pA.

d Overlay of the electrical response of the vacuole having the red-type TPC1 to 100 ms pulses of 300 pA, 600 pA and 900 pA.

e Dependency of the length of the post-stimulus plateau phase on the stimulus strength.

References

Allen, G.J., and Sanders, D. (1995). Calcineurin, a Type 2B Protein Phosphatase, Modulates the Ca2+-Permeable Slow Vacuolar Ion Channel of Stomatal Guard Cells. Plant Cell **7,** 1473-1483.

Bauer, H., Ache, P., Lautner, S., Fromm, J., Hartung, W., Al-Rasheid, K.A., Sonnewald, S., Sonnewald, U., Kneitz, S., Lachmann, N., Mendel, R.R., Bittner, F., Hetherington, A.M., and Hedrich, R. (2013). The stomatal response to reduced relative humidity requires guard cell-autonomous ABA synthesis. Curr Biol **23,** 53-57.

Bethke, P.C., and Russell, L.J. (1997). Reversible protein phosphorylation regulates the activity of the slow-vacuolar ion channel. The Plant Journal **11,** 1227–1235.

Beyhl, D., Hortensteiner, S., Martinoia, E., Farmer, E.E., Fromm, J., Marten, I., and Hedrich, R. (2009). The fou2 mutation in the major vacuolar cation channel TPC1 confers tolerance to inhibitory luminal calcium. Plant J **58,** 715-723.

Bonaventure, G., Gfeller, A., Rodriguez, V.M., Armand, F., and Farmer, E.E. (2007a). The fou2 gain-of-function allele and the wild-type allele of Two Pore Channel 1 contribute to different extents or by different mechanisms to defense gene expression in Arabidopsis. Plant Cell Physiol **48,** 1775-1789.

Bonaventure, G., Gfeller, A., Proebsting, W.M., Hortensteiner, S., Chetelat, A., Martinoia, E., and Farmer, E.E. (2007b). A gain-of-function allele of TPC1 activates oxylipin biogenesis after leaf wounding in Arabidopsis. Plant J **49,** 889-898.

Brelidze, T.I., Niu, X., and Magleby, K.L. (2003). A ring of eight conserved negatively charged amino acids doubles the conductance of BK channels and prevents inward rectification. Proc Natl Acad Sci U S A **100,** 9017-9022.

Bucchini, F., Del Cortona, A., Kreft, K., Botzki, A., Van Bel, M., and Vandepoele, K. (2020). TRAPID 2.0: a web application for taxonomic and functional analysis of de novo transcriptomes. bioRxiv doi: 10.1101/2020.10.19.345835.

Carpaneto, A., Cantu, A.M., and Gambale, F. (2001). Effects of cytoplasmic Mg2+ on slowly activating channels in isolated vacuoles of Beta vulgaris. Planta **213,** 457-468.

Choi, W.G., Toyota, M., Kim, S.H., Hilleary, R., and Gilroy, S. (2014). Salt stress-induced Ca2+ waves are associated with rapid, long-distance root-to-shoot signaling in plants. Proc Natl Acad Sci U S A **111,** 6497-6502.

Croll, T.I. (2018). ISOLDE: a physically realistic environment for model building into low-resolution electron-density maps. Acta Crystallogr D Struct Biol **74,** 519-530.

Dadacz-Narloch, B., Kimura, S., Kurusu, T., Farmer, E.E., Becker, D., Kuchitsu, K., and Hedrich, R. (2013). On the cellular site of two-pore channel TPC1 action in the Poaceae. New Phytol **200,** 663-674.

Dadacz-Narloch, B., Beyhl, D., Larisch, C., Lopez-Sanjurjo, E.J., Reski, R., Kuchitsu, K., Muller, T.D., Becker, D., Schonknecht, G., and Hedrich, R. (2011). A novel calcium binding site in the slow vacuolar cation channel TPC1 senses luminal calcium levels. Plant Cell **23,** 2696-2707.

Dickinson, M.S., Lu, J., Gupta, M., Marten, I., Hedrich, R., and Stroud, R.M. (2022). Molecular basis of multistep voltage activation in plant two-pore channel 1. Proc Natl Acad Sci U S A **accepted for publication**.

Dindas, J., Dreyer, I., Huang, S., Hedrich, R., and Roelfsema, M.R.G. (2021). A voltage-dependent Ca(2+) homeostat operates in the plant vacuolar membrane. New Phytol **230,** 1449-1460.

Dreyer, I., Sussmilch, F.C., Fukushima, K., Riadi, G., Becker, D., Schultz, J., and Hedrich, R. (2021). How to Grow a Tree: Plant Voltage-Dependent Cation Channels in the Spotlight of Evolution. Trends Plant Sci.

Evans, M.J., Choi, W.G., Gilroy, S., and Morris, R.J. (2016). A ROS-Assisted Calcium Wave Dependent on the AtRBOHD NADPH Oxidase and TPC1 Cation Channel Propagates the Systemic Response to Salt Stress. Plant Physiol **171,** 1771-1784.

Guo, J., Zeng, W., and Jiang, Y. (2017). Tuning the ion selectivity of two-pore channels. Proc Natl Acad Sci U S A **114,** 1009-1014.

Guo, J., Zeng, W., Chen, Q., Lee, C., Chen, L., Yang, Y., Cang, C., Ren, D., and Jiang, Y. (2016). Structure of the voltage-gated two-pore channel TPC1 from Arabidopsis thaliana. Nature **531,** 196-201.

Gutla, P.V., Boccaccio, A., De Angeli, A., Gambale, F., and Carpaneto, A. (2012). Modulation of plant TPC channels by polyunsaturated fatty acids. J Exp Bot **63,** 6187-6197.

Hedrich, R., and Neher, E. (1987). Cytoplasmic calcium regulates voltage-dependent ion channels in plant vacuoles. Nature **329,** 833-835.

Hedrich, R., and Marten, I. (2011). TPC1-SV channels gain shape. Mol Plant **4,** 428-441.

Hedrich, R., Mueller, T.D., Becker, D., and Marten, I. (2018). Structure and Function of TPC1 Vacuole SV Channel Gains Shape. Mol Plant **11,** 764-775.

Hedrich, R., Barbier-Brygoo, H., Felle, H., Flügge, U.I., Lüttge, U., Maathuis, F.J.M., Marx, S., Prins, H.B.A., Raschke, K., Schnabl, H., Schroeder, J.I., Struve, I., Taiz, L., and Ziegler, P. (1988). General mechanisms for solute transport across the tonoplast of plant vacuoles: a patch-clamp survey of ion channels and proton pumps. Botanica Acta **101,** 7-13.

Hille, B. (1971). The permeability of the sodium channel to organic cations in myelinated nerve. J Gen Physiol **58,** 599-619.

Jaslan, D., Böck, J., Krogsaeter, E., and Grimm, C. (2020). Evolutionary Aspects of TRPMLs and TPCs. Int J Mol Sci **21**.

Jaslan, D., Dreyer, I., Lu, J., O'Malley, R., Dindas, J., Marten, I., and Hedrich, R. (2019). Voltage-dependent gating of SV channel TPC1 confers vacuole excitability. Nat Commun **10,** 2659.

Jaslan, D., Mueller, T.D., Becker, D., Schultz, J., Cuin, T.A., Marten, I., Dreyer, I., Schonknecht, G., and Hedrich, R. (2016). Gating of the two-pore cation channel AtTPC1 in the plant vacuole is based on a single voltage-sensing domain. Plant Biol (Stuttg) **18,** 750-760.

Kintzer, A.F., and Stroud, R.M. (2016). Structure, inhibition and regulation of two-pore channel TPC1 from Arabidopsis thaliana. Nature **531,** 258-262.

Kintzer, A.F., and Stroud, R.M. (2018). On the structure and mechanism of two-pore channels. FEBS J **285,** 233-243.

Kintzer, A.F., Green, E.M., Dominik, P.K., Bridges, M., Armache, J.P., Deneka, D., Kim, S.S., Hubbell, W., Kossiakoff, A.A., Cheng, Y., and Stroud, R.M. (2018). Structural basis for activation of voltage sensor domains in an ion channel TPC1. Proc Natl Acad Sci U S A **115,** E9095-E9104.

Lagostena, L., Festa, M., Pusch, M., and Carpaneto, A. (2017). The human two-pore channel 1 is modulated by cytosolic and luminal calcium. Sci Rep **7,** 43900.

Latz, A., Becker, D., Hekman, M., Muller, T., Beyhl, D., Marten, I., Eing, C., Fischer, A., Dunkel, M., Bertl, A., Rapp, U.R., and Hedrich, R. (2007). TPK1, a Ca(2+)-regulated Arabidopsis vacuole two-pore K(+) channel is activated by 14-3-3 proteins. Plant J **52,** 449-459.

Lenglet, A., Jaslan, D., Toyota, M., Mueller, M., Muller, T., Schonknecht, G., Marten, I., Gilroy, S., Hedrich, R., and Farmer, E.E. (2017). Control of basal jasmonate signalling and defence through modulation of intracellular cation flux capacity. New Phytol.

Lewis, C.A. (1979). Ion-concentration dependence of the reversal potential and the single channel conductance of ion channels at the frog neuromuscular junction. J Physiol **286,** 417-445.

Nagai, T., Ibata, K., Park, E.S., Kubota, M., Mikoshiba, K., and Miyawaki, A. (2002). A variant of yellow fluorescent protein with fast and efficient maturation for cell-biological applications. Nat Biotechnol **20,** 87-90.

Navarro-Retamal, C., Schott-Verdugo, S., Gohlke, H., and Dreyer, I. (2021). Computational Analyses of the AtTPC1 (Arabidopsis Two-Pore Channel 1) Permeation Pathway. Int J Mol Sci **22**.

Neher, E. (1992). Correction for liquid junction potentials in patch-clamp experiments. Methods in Enzymology **207, ,** 9.

Nour-Eldin, H.H., Geu-Flores, F., and Halkier, B.A. (2010). USER cloning and USER fusion: the ideal cloning techniques for small and big laboratories. Methods Mol Biol **643,** 185-200.

Panzer, S., Brych, A., Batschauer, A., and Terpitz, U. (2019). Opsin 1 and Opsin 2 of the Corn Smut Fungus Ustilago maydis Are Green Light-Driven Proton Pumps. Front Microbiol **10,** 735.

Pei, Z.M., Ward, J.M., and Schroeder, J.I. (1999). Magnesium Sensitizes Slow Vacuolar Channels to Physiological Cytosolic Calcium and Inhibits Fast Vacuolar Channels in Fava Bean Guard Cell Vacuoles. Plant Physiol **121,** 977-986.

Peiter, E., Maathuis, F.J., Mills, L.N., Knight, H., Pelloux, J., Hetherington, A.M., and Sanders, D. (2005). The vacuolar Ca2+-activated channel TPC1 regulates germination and stomatal movement. Nature **434,** 404-408.

Perez, V., Wherrett, T., Shabala, S., Muniz, J., Dobrovinskaya, O., and Pottosin, I. (2008). Homeostatic control of slow vacuolar channels by luminal cations and evaluation of the channel-mediated tonoplast Ca2+ fluxes in situ. J Exp Bot **59,** 3845-3855.

Pottosin, II, Martinez-Estevez, M., Dobrovinskaya, O.R., and Muniz, J. (2005). Regulation of the slow vacuolar channel by luminal potassium: role of surface charge. J Membr Biol **205,** 103-111.

Pottosin, II, Martinez-Estevez, M., Dobrovinskaya, O.R., Muniz, J., and Schonknecht, G. (2004). Mechanism of luminal Ca2+ and Mg2+ action on the vacuolar slowly activating channels. Planta **219,** 1057-1070.

Pottosin, I., Olivas-Aguirre, M., Dobrovinskaya, O., Zepeda-Jazo, I., and Shabala, S. (2020). Modulation of Ion Transport Across Plant Membranes by Polyamines: Understanding Specific Modes of Action Under Stress. Front Plant Sci **11,** 616077.

Pottosin, I.I., I., T.L., Hedrich, R., and Schönknecht, G. (1997). Slowly activating vacuolar channels can not mediate Ca2+-induced Ca2+ release The Plant Journal **12,** 1387-1398.

Schindelin, J., Arganda-Carreras, I., Frise, E., Kaynig, V., Longair, M., Pietzsch, T., Preibisch, S., Rueden, C., Saalfeld, S., Schmid, B., Tinevez, J.Y., White, D.J., Hartenstein, V., Eliceiri, K., Tomancak, P., and Cardona, A. (2012). Fiji: an open-source platform for biological-image analysis. Nat Methods **9,** 676-682.

Schönknecht, G. (2013). Calcium Signals from the Vacuole. Plants (Basel) **2,** 589-614.

Schroeder, J.I., and Hedrich, R. (1989). Involvement of ion channels and active transport in osmoregulation and signaling of higher plant cells. Trends Biochem Sci **14,** 187-192.

Schulz-Lessdorf, B., and Hedrich, R. (1995). Protons and calcium modulate SV-type channels in the vacuolar-lysosomal compartment - Channel interaction with calmodulin inhibitors. Planta **197,** 655-671.

Schulze, C., Sticht, H., Meyerhoff, P., and Dietrich, P. (2011). Differential contribution of EF-hands to the Ca(2)(+)-dependent activation in the plant two-pore channel TPC1. Plant J **68,** 424-432.

Sheen, J. (2002). A transient expression assay using Arabidopsis mesophyll protoplasts. http://genetics.mgh.harvard.edu/sheenweb/ **Accessed October 10, 2020.**

Sun, Y.M., Favre, I., Schild, L., and Moczydlowski, E. (1997). On the structural basis for size-selective permeation of organic cations through the voltage-gated sodium channel. Effect of alanine mutations at the DEKA locus on selectivity, inhibition by Ca2+ and H+, and molecular sieving. J Gen Physiol **110,** 693-715.

Ward, J.M., and Schroeder, J.I. (1994). Calcium-Activated K+ Channels and Calcium-Induced Calcium Release by Slow Vacuolar Ion Channels in Guard Cell Vacuoles Implicated in the Control of Stomatal Closure. Plant Cell **6,** 669-683.

Webb, B., and Sali, A. (2016). Comparative Protein Structure Modeling Using MODELLER. Curr Protoc Bioinformatics **54,** 5 6 1-5 6 37.

Yoo, S.D., Cho, Y.H., and Sheen, J. (2007). Arabidopsis mesophyll protoplasts: a versatile cell system for transient gene expression analysis. Nat Protoc **2,** 1565-1572.